

Estimating hydrodynamic roughness in a wave-dominated environment with a high resolution acoustic Doppler profiler

Jessica R. Lacy,¹ Christopher R. Sherwood,² Douglas J. Wilson,³ Thomas A. Chisholm,⁴ and Guy R. Gelfenbaum¹

J. Lacy, U.S. Geological Survey, Coastal and Marine Geology, 345 Middlefield Road, MS-999, Menlo Park, CA 94025. (jlacy@usgs.gov)

C. Sherwood, U.S. Geological Survey, Coastal and Marine Geology, 384 Woods Hole Road, Woods Hole, MA 02543. (csherwood@usgs.gov)

D. Wilson, Imagenex Technology Corp., 209–1875 Broadway Street, Port Coquitlam, BC, V3C 4Z1 Canada. (dougw@ese.ogi.edu)

T. Chisholm, Oregon Graduate Institute, Department of Environmental Science and Engineering, 20000 NW Walker Road, Beaverton, OR 97006. (chisholm@ese.ogi.edu)

G. Gelfenbaum, U.S. Geological Survey, Coastal and Marine Geology, 345 Middlefield Road, MS-999, Menlo Park, CA 94025. (ggelfenbaum@usgs.gov)

¹U.S. Geological Survey, Menlo Park,
California

²U.S. Geological Survey, Woods Hole,
Massachusetts

³Imagenex, Port Coquitlam, BC, Canada

⁴Oregon Graduate Institute, Beaverton,
Oregon

Abstract. Hydrodynamic roughness is a critical parameter for characterizing bottom drag in boundary layers, and it varies with grain size, bedforms, and saltating sediment. We used velocity profiles in the bottom boundary layer measured with a high resolution acoustic Doppler profiler (PCADP) to estimate hydrodynamic roughness and bedform height. The data were collected on the ebb-tidal delta off Grays Harbor, Washington in a mean water depth of 9 m. Significant wave height ranged from 0.5 to 2 m. Velocities measured by the PCADP compared well to those measured by an acoustic Doppler velocimeter mounted on the same tripod. Friction velocity due to current u_{*c} and apparent bottom roughness z_{0a} were determined from the PCADP burst mean velocities using the law of the wall. Bottom roughness \hat{k}_B was estimated using the Grant-Madsen model for wave-current interaction (GM) iteratively until the model u_{*c} converged with values from the log fits. \hat{k}_B varied inversely with wave orbital diameter d_o . Friction velocity at the bed due to waves and current u_{*cw} was calculated using GM and a time-varying k_B based on the relationship between \hat{k}_B and d_o , and differed significantly from u_{*cw} using a constant k_B . Bedform height $\hat{\eta}$ was estimated from k_B after accounting for the contribution of saltating sediment. $\hat{\eta}$ compared favorably to ripple heights predicted by empirical models, as well as to bedforms seen in sonar images collected during the experiment.

1. Introduction

Bottom shear stress and hydrodynamic roughness are essential parameters in determining sediment resuspension and transport, but they are difficult to measure directly. In a fully developed unidirectional flow, friction velocity (which is directly related to bottom shear stress) and hydrodynamic roughness can be determined from velocity profiles in the bottom boundary layer, using the law of the wall. In a combined wave-current flow, the thin wave boundary layer interacts directly with the bottom roughness, and the near-bed turbulence generated by the waves increases the apparent hydrodynamic roughness that influences the current boundary layer. Bottom shear stress and bottom roughness cannot be estimated directly from measurements made outside the wave boundary layer. Several models of wave-current interaction have been developed to estimate bottom shear stress from measurements taken outside the wave boundary layer (e.g., [Jonsson, 1966; Smith, 1977; Grant and Madsen, 1979; Styles and Glenn, 2000]). These models require an estimate of physical bottom roughness k_B as an input. k_B is difficult to estimate and changes over time, because it is influenced by grain size, bedform geometry, and near-bed sediment transport. Methods for estimating k_B for movable beds of well-sorted sands have been proposed by Grant and Madsen [1982], Nielsen [1992], Wikramanayake and Madsen [1991], Xu and Wright [1995], Li and Amos [1998], and Styles and Glenn [2002], among others, but experimental verification of these techniques in the field has been difficult because it requires good data for both physical bottom configuration and flow conditions.

The accuracy of estimates of friction velocity and hydrodynamic roughness from velocity profiles depends strongly on the number of velocity measurements in the bottom boundary layer [Gross and Nowell, 1983]. In arrays of individual current meters, this number is

limited by physical constraints in positioning the current meters. The recent development of pulse-to-pulse coherent acoustic Doppler profilers promises a high-resolution, high-frequency (1–2 Hz), non-intrusive, and accurate method for measuring velocity profiles in the bottom boundary layer [*Lhermite and Serafin*, 1984; *Zedel et al.*, 1996]. Field testing of this technology, particularly in wavy environments, has been limited.

In this paper we present estimates of bottom roughness \hat{k}_B inferred from velocity profiles in the bottom boundary layer using the Grant-Madsen model for wave-current interaction (GM) [*Grant and Madsen*, 1979; *Madsen*, 1994] in an inverse mode. We applied the inverse method to a data set of more than 800 bursts collected over two months using a pulse-coherent acoustic Doppler profiler (PCADP). Friction velocity due to currents u_{*c} and apparent bottom roughnesses z_{0a} are estimated from the profiles and used as inputs to the inverse model. Time-varying bottom roughness is calculated based on the relationship between wave orbital diameter and estimated \hat{k}_B , and used as an input to GM to predict friction velocity at the bed u_{*cw} . Bedform heights are estimated from the inferred bottom roughnesses, compared to those predicted by empirical formulae, and related to sonar images of the bed. Wave conditions were energetic during the study and ripples were small (wavelength ~ 0.1 m), contrasting with the lower-energy conditions and large orbital ripples studied by *Traykovski et al.* [1999] and *Styles and Glenn* [2002].

2. Methods

2.1. Study Site

The study was conducted off the coast of southwest Washington outside of Grays Harbor during the summer of 2001 (Figure 1). The Washington coast is characterized by rough wave conditions and large tides, with tidal range exceeding 3 m during spring tides. In

Figure 1

winter, significant wave heights measured at the CDIP buoy (Figure 1) are frequently greater than 4 m, and exceed 8 m during major storms. In summer, significant wave heights are typically 1–2 m, and reach 4 m during periods of strong southerly winds. The data described in this paper were obtained on the inner shelf just outside the surf zone (mean depth of 9 m) on the northern flank of the Grays Harbor ebb-tidal delta (MIA and MIB, Figure 1), as part of a study linking seasonal changes in sediment transport around the ebb-tidal delta off Grays Harbor to erosion and accretion on the adjacent coast. Sediment at this site (and over most of the ebb-tidal delta and adjoining beaches) is well-sorted fine sand comprised of quartz, feldspar, and metamorphic and volcanic rock fragments, typical of the coarser fraction of material delivered by the Columbia River. Sediment in grab samples from MIA had a D_{85} of 0.18 mm.

2.2. Data Collection

Two instrumented tripods were deployed to measure currents, waves, and suspended sediment, and to record sonar images in the bottom boundary layer. The tripods were deployed May 4, 2001, and recovered July 11, with one turn-around June 6–8 to change batteries, recover data, and clean sensors. At station MIA a 1.5 MHz Sontek PCADP was mounted on the tripod looking downwards from a height of 130 cm, to measure velocity profiles in the bottom meter above the bed. The PCADP measured velocity in eight 10-cm (nominal) cells, at 1 Hz. Other sampling parameters for the PCADP are shown in Table 1. A Paros Scientific Digiquartz pressure sensor connected to the PCADP measured pressure at 1 Hz. An Aquatec acoustic backscatter sensor (ABS) with 1, 2.5, and 5 MHz transducers sampled at 1 Hz in 128 1-cm bins to measure near-bed profiles of suspended

sediment concentration. Both the PCADP and ABS sampled for 20-minute bursts every hour.

During the first deployment (May 4–June 6) two synchronized Sontek Field acoustic Doppler velocimeters (ADVF) were mounted on the tripod with sampling volumes at 72 cm height, separated horizontally by 90 cm, and sampled at 20 Hz for a 20-minute burst every 120 minutes. Data from the ADVFs, which measure three components of velocity at one location, were used to estimate shear stress using the eddy correlation technique [Sherwood and Lacy, manuscript in preparation]. During the turn-around, one of the ADVFs was damaged and was not redeployed. As a result, the primary purpose of the remaining ADVF shifted from turbulence measurement to PCADP verification. During the second deployment (June 8–July 11) the sampling frequency was reduced to 10 Hz, and the height of the sampling volume was 78 cm. D&A Instruments optical backscatter sensors (OBS) measured suspended sediment concentration at six heights above the bed during deployment 1 and at four heights during deployment 2.

A sonar system, mounted on a second tripod (station MIB) approximately 50 m north from MIA, collected images of the bottom [Hay and Wilson, 1994]. An Imagenex model 858 controlled two model 855 sonar heads operating at 2.25 MHz. One of the sonar heads emitted a fan beam and rotated 360° about a vertical axis, producing a plan-view image of the sea floor. The other head emitted a narrow conical beam and rotated 360° about a horizontal axis, producing a profile of the bed. The effective range of the imaging head, a function of beam spreading, signal-to-noise ratio, and the angle between the beam and the bed, was 4–5 meters. The spacing of the returns from the profiling beam ranged from about 1.6 cm directly under the transducer to about 4.3 cm at 2 m from the transducer. A

Sontek Ocean acoustic Doppler velocimeter (ADVO) on the same tripod sampled velocity and pressure at 2 Hz for a 20-minute burst every hour.

The sonars collected images every 2 hours. Each scan took 45 seconds, much longer than individual resuspension events, which occur at wave periods. Images were constructed from averages of one or two scans. An image enhancement algorithm calculated averages of all values equidistant from the transducer, and normalized each value by subtracting the mean and dividing by the standard deviation.

Profile images typically contain a section of large return caused by suspended sediment, which ends at the bed, followed by a quieter section corresponding to the region below the bed. Bed elevation was determined from the profile image by comparing low-pass filtered returns to the maximum return of each ping, working inward from below the bottom. The first return exceeding 75% of the maximum value was used to identify the elevation of the bed. The approximately 155 bottom elevations were interpolated to 400 elevations spaced 1 cm apart. To check for false bottoms, elevations were compared to adjacent values. The angle of repose of sand is at most 45° , which corresponds to an elevation difference of 1 cm between adjacent points. Therefore, any point whose elevation differed by more than 1 cm from adjacent points was adjusted to an elevation 1 cm from the preceding point.

2.3. Conditions During the Experiment

Winds, waves, and currents shifted from spring to summer conditions over the course of the experiment (Figure 2). Wind stress and wave height decreased as the summer pro-

Figure 2

winds. There were several periods of strong winds from the south that produced wave heights up to 2 m, northward currents, and brief veering of the wave propagation direction towards the north. The longest such event was from May 15 to 17. Despite the decrease in wave energy as the summer progressed, the calculated grain roughness Shields parameter [Nielsen, 1992] shows that the threshold for sediment motion (0.05) was exceeded throughout the experiment (Figure 3). Wave velocities dominated currents: the median of the ratio of mean current 50 cm above the bed to bottom orbital velocity was 0.23, and the 90th percentile was 0.65. Bottom orbital velocity was calculated as

Figure 3

$$u_b = \sqrt{2 \int S_{uv}(\omega) d\omega} \quad (1)$$

where S_{uv} is the spectrum of near-bottom velocity as a function of wave frequency ω .

3. Results

3.1. Estimates of u_{*c} and z_{0a} From Velocity Profiles

The velocity profile in the bottom boundary layer of a steady flow is governed by the law of the wall:

$$u(z) = u_* \frac{1}{\kappa} \ln \left(\frac{z}{z_0} \right) \quad (2)$$

where u is horizontal velocity, u_* is friction velocity, $\kappa = 0.41$ is the Von Kármán constant, z is the height above the bed, and z_0 is the hydrodynamic roughness. Friction velocity u_* and z_0 can be found from a plot of mean velocity vs. the logarithm of z , which has slope κ/u_* and y -intercept z_0 . The boundary layer created by steady currents is fully developed and thus typically extends for meters above the bed, or to the height of a change in density. Wave boundary layers, on the other hand, have only a few seconds to develop and thus are much thinner, typically less than 10 cm. In a combined wave and

current flow, the influence of the wave boundary layer on the current boundary layer can be modeled as an increase in roughness [*Grant and Madsen*, 1979]. Mean velocities above the wave boundary layer are logarithmically distributed with respect to depth; however, the y -intercept occurs at a higher elevation when waves are present. A modified form of equation 2 holds for the current boundary layer in wavy flows:

$$u(z) = u_{*c} \frac{1}{\kappa} \ln \left(\frac{z}{z_{0a}} \right) \quad (3)$$

where z_{0a} is known as the apparent roughness, and u_{*c} denotes the friction velocity due to the current, as distinguished from the friction velocity at the bed due to the combination of the waves and current, u_{*cw} .

The velocity profiles measured by the PCADP typically follow the expected logarithmic bottom boundary layer profile in the five bottom bins (farthest from the transducers), but in the cells closest to the transducer velocities are lower than expected (Figure 4). In addition, vertical velocities are frequently higher in magnitude than is reasonable, with increasing magnitude closer to the transducers. Velocities measured by the PCADP in cell 5 were compared to those measured by the ADVF (whose sampling volume fell within the range of cell 5) to confirm the accuracy of the PCADP measurements and of ambiguity-error correction at this height.

Figure 4

Bottom orbital velocity calculated from the ADVF and PCADP data are strongly correlated ($R^2 > 0.92$, $N = 1195$). Time series of bottom orbital velocities and burst mean speeds calculated from the two instruments also show good agreement (Figure 5). The PCADP accurately measured bottom orbital velocities up to 100 cm/s (well above the ambiguity velocity of 65 cm/s) and burst mean speeds up to 40 cm/s. The error in the bottom orbital velocity calculated by the PCADP, $u_{b,PCADP} - u_{b,ADVF}$, was within ± 8

Figure 5

cm/s throughout the deployment (Figure 5b). The absolute value of the percent difference between the bottom orbital velocity measured by the two instruments had a mean of 4.0% and a standard deviation of 3.4%. The error in burst mean speed, $\bar{u}_{\text{PCADP}} - \bar{u}_{\text{ADVF}}$, was within ± 2 cm/s for more than 98% of the bursts and was always within ± 6 cm/s (Figure 5d). The absolute value of the percent difference between the burst mean speeds (for values greater than 5 cm/s) had a mean of 7.3% and a standard deviation of 7.2% ($N = 823$). The error in u_b is more often positive than negative, indicating a slight bias towards higher PCADP estimates of u_b (mean error = 1.2 cm/s). The estimates of burst mean speed do not appear to be biased. Lacy and Sherwood [manuscript in preparation] discuss the comparison of the PCADP and ADVF data in further detail.

In Figure 4, velocities from each cell are plotted at the midpoint of the cell, although the velocity measured by the PCADP is an average for the depth interval of the cell. In a logarithmic profile, the depth-averaged velocity is not equal to the velocity at the midpoint, and this difference increases as the shear in the profile increases, approaching the bed. However, for this data set the difference is negligible. If we assume that the velocity profile is logarithmic and the lowest cell starts 10 cm above the bed, and set $u_{*c} = 2$ cm/s and $z_{0a} = 1$ cm, then the depth-averaged velocity for the cell is 13.117 cm/s and the velocity at the midpoint (15 cm) is 13.21 cm/s. The depth-averaged velocity occurs at 14.717 cm rather than at 15 cm, a difference that is less than the accuracy in measuring the distance to the bottom (~ 1 cm).

Friction velocity due to current u_{*c} and apparent roughness z_{0a} were calculated by fitting the PCADP burst mean velocity profiles to equation 3. The PCADP measures the distance from the transducer to the bed (accuracy of ± 1 cm) at the beginning of each

burst. The distance of the PCADP from the bed varied somewhat over the course of the deployment due to settling and periodic erosion. For each burst, the mean of the distance to bottom measured by the three beams was used to determine the z -locations of the midpoints of the cells for the fitting of the data to a logarithmic curve. The bottom five cells were always used, and cells above that were sequentially added if they increased the correlation coefficient (R^2) between the data and the fitted logarithmic curve. The log fits were used to estimate u_{*c} and z_{0a} if the following criteria were met: $R^2 \geq 0.96$, and burst mean speed greater than 5 cm/s at 50 cm above the bed (cell 5). 407 out of 769 bursts in deployment 1 and 466 of the 810 bursts in deployment 2 met the criteria. The restriction on R^2 values was enforced to limit the error in the estimates of u_{*c} and z_{0a} .

3.2. Uncertainty in u_{*c} and z_{0a}

Two factors were taken into account in estimating the error in u_{*c} and z_{0a} : uncertainty in the log fits and variation in the distance to bottom measured by the three beams of the PCADP. The $(1 - \alpha)$ confidence interval on the estimate of u_{*c} from a log fit is calculated [Neter *et al.*, 1985] as

$$u_{*c} \pm t_{(1-\alpha/2, n-2)} \sqrt{\frac{\text{MSE}}{\sum (u(z) - \bar{u})^2}} \quad (4)$$

where t is the t-statistic, n is the number of measurements, and $\text{MSE} = \sum (Y_i - \hat{Y}_i)^2 / (n - 2)$ is the mean square error. The quantity inside the square root can be expressed in terms of R^2 and n [Gross and Nowell, 1983]. For $R^2 = 0.96$ and $n = 5$, the 90% confidence interval on u_{*c} is $\pm 40\%$. Actual errors were lower: the median error for the 873 calculated values of u_{*c} due to uncertainty in the log fits was 8%, and 90% of the values had error less than 18%. The maximum error was 27.6%. The error in $\ln(z_{0a})$ is calculated as the error on the

y -intercept of a regression, and is approximately $\pm 55\%$ for $n = 5$ and $R^2 = 0.96$ [*Gross and Nowell*, 1983]. There are two primary reasons for the large errors in estimating z_{0a} : it is estimated by extrapolating outside the range of depths used in fitting the logarithmic curve and it is calculated by taking the exponential of the error in $\ln(z_{0a})$.

The ability of the PCADP to measure the distance to the bottom has the benefit of limiting the uncertainty in the heights of the velocity measurements. Nevertheless some uncertainty remains due to variation in the distance to bottom between the three beams caused by bedforms or a sloping bed, as well as error in the distance measurements. The PCADP uses backscatter from all three beams to calculate three orthogonal components of velocity, based on the assumption that velocities in the region occupied by the three beams vary only with depth. When the bed is not flat, velocities from different heights above the bed are combined, particularly in the lowest depth cell where the beams are farthest apart (~ 0.5 m separation in our experiment). To account for this source of error, we evaluated u_{*c} and z_{0a} using z -locations based on the minimum (z_{\min}) and the maximum (z_{\max}) of the three distances to bottom measured by the PCADP for each burst, after correction for pitch and roll. The difference between z_{\max} and z_{\min} ranges from 0.9 to 8.5 cm, with a median of 2.9 cm. We then estimated the combined error from uncertainty in the log fits and irregularity in the bed to extend from the upper 90% confidence interval on the fit using z_{\max} to the lower 90% confidence interval using z_{\min} . The median of the combined error in u_{*c} is 13%, 90% of the errors are less than 25%, and the maximum error is 45%. The median combined error in z_{0a} is -45% to $+74\%$ (90th percentile -70% to $+180\%$).

3.3. Comparison with GM

Time series of the estimated u_{*c} and z_{0a} are shown in Figure 6, with error bars combining the two sources of uncertainty just described. Figure 6 also shows a range of u_{*c} and z_{0a} predicted by GM. GM uses a reference velocity, reference depth, bottom orbital velocity, the angle between waves and currents, and the inner (equivalent Nikuradse) roughness k_B to predict u_{*c} , z_{0a} , and u_{*cw} . The maximum bottom shear stress over a wave period, the relevant parameter for predicting sediment resuspension, can be calculated from u_{*cw} . For a steady, fully turbulent flow over a flat bed, k_B is equal to the grain size diameter, and the hydrodynamic roughness is $z_0 = k_B/30$ [Nielsen, 1992]. However, inner roughness is influenced by bedforms and other factors, and thus changes over time (see Discussion). Figure 6 shows a range of predictions with a lower bound based on $k_B = 0.2$ mm and an upper bound based on $k_B = 5$ cm, to represent the range of reasonable values of k_B ($D_{85} = 0.18$ mm). Both u_{*c} and z_{0a} from the log fits fall within the predicted range most of the time. They are greater than the model predictions during the first week of the second deployment, and z_{0a} is underestimated at a number of times. Comparison with the time series of bottom orbital velocity in Figure 6a shows that u_{*c} increased during periods of larger waves (May 9, May 15–17, June 28–29). The section of the time series in Figure 7 shows that the calculated values of u_{*c} follow the tidal signal in the predictions and that the predicted response to the event of May 15–17 is well reproduced.

Figure 6

Figure 7

Sediment resuspended by waves can create stratification in the bottom boundary layer, which reduces turbulent mixing and u_{*c} . The influence of stratification is not taken into account by GM. To determine the importance of stratification on u_{*c} , we used a model of wave-current interaction in the bottom boundary layer developed by Wiberg

et al. [1994]. We ran the model both with stratification and without (Figure 8). The influence of stratification was greatest during peaks of both burst mean speed and bottom orbital velocity, when stratification decreased the predicted u_{*c} by approximately 0.5 cm/s. During these energetic periods, bedforms tend to wash out and k_B should be low. The combination of low k_B and lack of stratification in GM could account for the overprediction of u_{*c} between May 15 and 17 (Figure 7). Most of the time, when wave energy was lower, the influence of stratification on u_{*c} was less than 0.2 cm/s. An error of this magnitude is not significant compared to the uncertainty introduced in the GM predictions by the range of possible k_B values.

Figure 8

3.4. Bedform Categories in Sonar Images

The sonar images (Figure 9) show two distinct length scales of variation in bed elevation, with wavelengths of ~ 1 m and ~ 10 cm. A time series of bed elevation profiles shows large-scale bedforms or megaripples that were often stable for several days at a time (Figure 10). In May, bedforms with wavelengths of about 1 m occurred when waves were approximately 1.5 m high, and appear to wash out during much larger or smaller wave conditions. In June, a scour pit formed adjacent to the tripod leg (seen on the right side of Figure 9) under approximately 1.5 m wave conditions. The heights of the small-scale bedforms or ripples were small due to the small grain size and energetic wave conditions. Ripple heights are not well resolved in the bed-elevation profiles, but ripple wavelength can be determined from the plan-view images. The average wavelength in 27 scans of mostly linear ripples in May was 9.4 cm (s.d. = 1.5 cm).

Figure 9**Figure 10**

Bedforms were categorized into four types by examining the plan-view images: rippled, irregular, megaripples, and flat bed. This categorization of bedforms that occur in

progressively more energetic conditions follows *Clifton* [1976]. Rippled beds had clearly identifiable linear features in the scan profile. Irregular ripples had similar texture to linear ripples but lacked long crests. Megaripples presented a smoother and lighter appearance in the scans but with some larger-scale irregularity. Flat bed appeared similar to megaripples but lacked large-scale irregularity and had a flat profile. Clifton also reported the occurrence of cross-ripples between irregular ripples and megaripples; such ripples were not distinguishable in the sonar records. The categorization was completed without considering other data. Comparison with wave height shows that bedform type corresponded consistently with wave energy, and provides some confirmation of the categorization (Figure 11). Most of the time the bedforms were irregular ripples or megaripples. Flat bed only developed during the most energetic period of the study, on May 15.

Figure 11

4. Discussion

Bottom drag in a steady turbulent flow over a sandy bed is a combination of skin friction associated with grain roughness and form drag caused by ripples, dunes, or biogenic features. In addition, when sediment is mobile, as it was throughout the experiment (Figure 3), momentum is extracted from the flow and transferred to saltating grains, effectively increasing the bottom drag. The overall length scale for bed roughness is $k_B = 30z_0$. The contribution of these three factors is generally treated as additive, so that $k_B = k_N + k_{ST} + k_{BF}$, where k_N is the Nikuradse grain roughness or length scale, k_{ST} is the saltation roughness length scale, and k_{BF} is the bedform roughness length scale [Smith, 1977; Cacchione and Drake, 1990]. For fully rough flow over a flat bed, k_N is equal to a representative grain diameter. Roughness associated with saltating sediment k_{ST} is a function of grain size and transport stage [Wiberg and Rubin, 1989]. Bedform

roughness k_{BF} is usually estimated by assuming some equilibrium bed geometry for the flow conditions and then relating z_0 to ripple height and steepness [Grant and Madsen, 1982]

The combined length scale k_B is an input parameter in GM wave-current calculations to estimate u_{*c} , z_{0a} , and τ_b , but, of course, k_B is actually a function of τ_b , because bottom shear stress causes bedload transport and determines bedform geometry. As shown by Figure 6, models like GM are very sensitive to k_B (or z_0), yet the choice of an appropriate value of k_B to input to GM is problematic. Actual bottom conditions are usually unknown and may lag in their response to time-varying forcing, and bottom roughness parameterizations are based on uncertain empirical relationships.

4.1. Inverse Estimate of Bed Roughness

We used GM to estimate \hat{k}_B , which is ordinarily an input parameter, for each burst. This approach was possible because we had estimates (from the log fits) of parameters predicted by GM, u_{*c} and z_{0a} . We solved GM iteratively, allowing \hat{k}_B to vary (between 10^{-5} and 0.4 m) until the predicted u_{*c} converged with the value determined from the log fits. Similar approaches have been used by Madsen *et al.* [1993], Xu and Wright [1995], and Styles and Glenn [2002]. The \hat{k}_B estimates were discarded unless the predicted u_{*c} converged to within 2% of the log-fit value in fewer than 20 iterations and the resulting \hat{k}_B was greater than one quarter the grain size. 788 of the 873 bursts with calculated u_{*c} met these criteria (347 of 407 in deployment 1 and 441 of 466 in deployment 2).

The time series of \hat{k}_B (Figure 12) shows that bed roughness ranged three orders of magnitude (from 10^{-4} to 10^{-1} m). The error in \hat{k}_B was estimated by requiring the iterative solution of GM to converge to the upper and lower bounds of the error estimated for u_{*c}

Figure 12

for each burst. \hat{k}_B was large when waves were smallest (May 11–14, June 8–19, June 30–July 6), and minimum \hat{k}_B occurred during periods of greatest wave energy (May 9, May 15–17, June 22, June 29).

This method of estimating bottom roughness depends on both the specific assumptions of GM and the accuracy of the data used in calculating u_{*c} . At some times the \hat{k}_B estimates are highly variable and at others they are fairly constant. High variability can be produced either by rapid changes in forcing or large uncertainty in the predictions. Bedforms typically respond rapidly to changes in hydrodynamic forcing, but the two are not always in equilibrium. Ripples produced by earlier more energetic conditions can persist after bottom shear stress drops below the threshold required for sediment movement [Drake *et al.*, 1992]. The Shields parameter shows that shear stress exceeded the threshold for sediment motion (0.05) throughout the deployment (Figure 3). Nevertheless, some lag time between hydrodynamic forcing and bedform response is expected, and is not taken into account by GM. Another limitation of the model is that it neglects the influence of stratification, although this was only important during times of high wave energy (Figure 8). In addition, when orbital velocities were high, noise in the velocity measurements increased due to higher levels of turbulence and more frequent ambiguity errors, so the uncertainty in the log fits was greater.

Our goal in estimating k_B is to determine the appropriate input value to models such as GM, to calculate bottom shear stress. While the qualitative behavior of the \hat{k}_B 's appears to be correct, the values are too noisy to use as a model input. We used the observed dependence of \hat{k}_B on wave orbital diameter to develop a smoothly varying predictive equation for k_B . Wave orbital diameter was calculated as $d_o = u_b \cdot T/\pi$, where u_b is

bottom orbital velocity and T is the representative wave period. The 788 bursts for which \hat{k}_B was calculated were divided into six groups based on the magnitude of d_o , and the geometric mean of the estimated \hat{k}_B 's was calculated for each group. A plot of the geometric means vs. the mean of each interval of d_o shows a logarithmic relationship between the two parameters (Figure 13). The least-squares fit line between the logarithms of the two parameters ($R^2 = 0.979$, 90% confidence interval on the slope of ± 0.155) is

Figure 13

$$k_{Bpred} = \exp[-5.4 - 2.3 \ln(d_o)] \quad (5)$$

With this equation k_{Bpred} can be estimated for all bursts. The resulting time series of k_{Bpred} preserves the large-scale temporal pattern in the \hat{k}_B values calculated for each burst, but has a narrower range and is less noisy (Figure 14). k_{Bpred} does not correspond well to the \hat{k}_B 's in the first week of the second deployment, the same period that had unusually high u_{*c} 's estimated from the log fits (Figure 6). During this period roughness may depend on factors other than orbital diameter.

Figure 14

Friction velocity due to waves and current u_{*cw} was calculated with GM, using the time series of k_{Bpred} (Figure 15). The time-varying k_{Bpred} produced u_{*cw} 's that were at times 50% higher, and at times 25% lower, than those calculated from a constant k_B of 0.5 cm (the geometric mean of k_{Bpred}). The effect on bottom shear stress is even greater because τ is proportional to u^2 . These results show that it is critical to account for the time-varying nature of k_B in estimating bottom shear stress and resuspension. While a parameterization of k_B based on wave energy alone (such as ours) does not account for all sources of variation in k_B , it produces much more realistic results than a constant k_B .

Figure 15

4.2. Estimates of Bedform Heights

We estimated bedform height η from \hat{k}_B to compare with the results from the sonar images, as a verification of the estimates of \hat{k}_B . Estimated η were also compared with predicted heights from three empirical ripple models. In estimating η we accounted for the contribution of saltating sediment to \hat{k}_B , to differentiate roughness caused by saltating sediment from that created by bedforms \hat{k}_{BF} . In calculating η from \hat{k}_{BF} , we distinguished between classes of ripples with different geometric characteristics.

Ripples have been categorized into three types based on wave energy and grain size: orbital, which occur when the ratio of wave orbital diameter to grain size is low; anorbital, which occur when this ratio is high; and suborbital, which occur during the transition from orbital to anorbital [*Clifton and Dingler*, 1984; *Wiberg and Harris*, 1994]. In the laboratory, *Clifton and Dingler* [1984] found that orbital ripples occur for $d_o/D < 2000$ and anorbital ripples occur when $d_o/D > 5000$. *Wiberg and Harris* [1994] found that the transition from orbital to suborbital occurs at $d_o/D = 1754$ and the transition to anorbital ripples occurs at $d_o/D = 5587$. The ratio of d_o to grain size shows that conditions throughout the deployment were too energetic for orbital ripples (Figure 16). During May, when large wave events occurred more frequently, predicted ripple type is suborbital approximately half of the time and anorbital the other half, while in June suborbital ripples are predicted most of the time.

Figure 16

Orbital ripples have wavelength proportional to the orbital diameter ($\lambda = 0.65 d_o$) and a constant steepness $\eta/\lambda = 0.17$ [*Nielsen*, 1981; *Wiberg and Harris*, 1994]. For anorbital ripples, wavelength is a function of grain size and is independent of orbital velocity, and can be estimated as $\lambda = 535 D$. Anorbital ripples have a steepness η/λ no greater than

0.12; ripple height and steepness decrease with increasing wave energy. At the study site predicted anorbital wavelength is $\lambda = 9$ cm using $D_{85} = 0.18$ mm, and anorbital ripple height η should not exceed 1.08 cm, based on the equations in *Wiberg and Harris* [1994]. This predicted wavelength is consistent with the average wavelength of linear ripples of 9.4 cm estimated from the sonar images in May.

Hydrodynamic roughness due to saltating sediment z_{0ST} was calculated based on the formulations by Dietrich, and Wiberg and Smith [*Wiberg and Rubin*, 1989]. Both formulations express z_{0ST} as a function of grain size, transport stage τ_b/τ_c , where τ_b is the bed shear stress and τ_c is the critical shear stress for sediment motion, and an empirically derived parameter. These two formulations showed the best agreement with data among those reviewed by Wiberg and Rubin. Roughness due to saltating sediment $\hat{k}_{ST} = 30z_{0ST}$ accounted for between 0.2 and 1 mm of \hat{k}_B (Figure 17), with maximum values when wave energy is high. Estimated \hat{k}_B is low when wave energy is high, so at these times (May 15–20, June 3, June 29) \hat{k}_{ST} is comparable to (or in some cases greater than) \hat{k}_B . The contribution of \hat{k}_{ST} was negligible for $\hat{k}_B > 2$ mm.

Figure 17

Bottom roughness due to bedforms was estimated as $\hat{k}_{BF} = \hat{k}_B - \hat{k}_{ST}$, assuming grain roughness k_N is negligible when bedforms are present. Bedform height η was calculated from the relationship between ripple height, steepness, and bedform bottom roughness proposed by *Grant and Madsen* [1982]:

$$k_{BF} = 27.7 \eta \frac{\eta}{\lambda} \quad (6)$$

In applying this equation, we assumed a constant steepness of 0.15 for suborbital or orbital ripples and a constant wavelength of $\lambda = 0.1$ m for anorbital ripples. Ripples with predicted height $\hat{\eta}$ less than 1 cm ($\hat{k}_{BF} < 0.04$ m) were treated as anorbital. The resulting

equation for predicting ripple height is:

$$\begin{aligned}\hat{\eta}_{\text{ano}} &= \sqrt{0.0036 \hat{k}_{\text{BF}}} & \hat{k}_{\text{BF}} \leq 0.04 \text{ m} \\ \hat{\eta}_{\text{sub}} &= \hat{k}_{\text{BF}}/4 & \hat{k}_{\text{BF}} > 0.04 \text{ m}\end{aligned}\tag{7}$$

Nielsen [1992] proposed a constant of 8 rather than 27.7 in equation 6. In that case the estimated ripple heights are 3.3 times larger for suborbital or orbital ripples and 1.9 times larger for anorbital ripples.

The time series of $\hat{\eta}$ obtained from equation 7 shows that $\hat{\eta}$, like \hat{k}_{B} , is inversely related to wave energy (Figure 16). The error bars on $\hat{\eta}$ in Figure 16c are based on the uncertainty in \hat{k}_{B} . For cases with $\hat{k}_{\text{ST}} > \hat{k}_{\text{B}}$, $\hat{\eta}$ was set equal to the grain size, producing the set of points in Figure 16c on the dashed line at D_{85} . This occurred when wave orbital velocity was highest, bedforms were small, and hydrodynamic roughness was controlled by \hat{k}_{ST} .

4.3. Comparison with Models

The $\hat{\eta}$ estimates are compared to predictions of ripple height based on *Nielsen* [1981], *Wiberg and Harris* [1994], and *Styles and Glenn* [2002] in Figure 18. All three predictive relationships are based on analysis of field and laboratory data. Nielsen derived expressions for the ratio of ripple height to wave semi-excursion $A = d_o/2$ that are a function of the mobility number $\psi = u_b^2/(s-1)gD$ alone, by considering only the case where the ratio of sediment to water density is $s = 2.65$ (quartz sand). Nielsen developed equations for η/A for field and laboratory data, and recommends use of the field equation for $\psi > 10$:

$$\frac{\eta}{A} = \begin{cases} 21\psi^{-1.85} & \psi > 10 \\ 0.275 - 0.022\sqrt{\psi} & \psi \leq 10 \end{cases}\tag{8}$$

In this experiment, 4.2% of the bursts have $\psi < 10$.

According to *Wiberg and Harris*, orbital ripples are characterized by a height that is greater than the wave boundary-layer thickness, while the height of anorbital ripples is

Figure 18

much less than the wave boundary-layer thickness. Wiberg and Harris found that ripple steepness is strongly related to d_o/η , which serves as an estimate of the ratio of wave boundary-layer thickness to ripple height. For $d_o/\eta > 10$,

$$\frac{\eta}{\lambda} = \exp \left[-0.095 \left(\ln \frac{d_o}{\eta} \right)^2 + 0.442 \ln \frac{d_o}{\eta} - 2.28 \right] \quad (9)$$

which can be solved iteratively for η , using $\lambda = 535D$. For $d_o/\eta \leq 10$ (orbital ripples), ripple height is estimated from $\eta/\lambda = 0.17$ and $\lambda = 0.62$.

Styles and Glenn recalibrated the relationships for predicting η and λ developed by *Wikramanayake and Madsen* [1991] by including the data used by *Wiberg and Harris* [1994] and the data of *Traykovski et al.* [1999], producing

$$\frac{\eta}{A} = \begin{cases} 0.30(\psi/S_*)^{-0.39} & \psi/S_* < 2 \\ 0.45(\psi/S_*)^{-0.99} & \psi/S_* \geq 2 \end{cases} \quad (10)$$

where $S_* = (D/4\nu)\sqrt{(s-1)gD}$ and ν is the kinematic viscosity of water. For our data set ψ/S_* is greater than 2 for all except one burst with $\psi/S_* = 1.97$.

The temporal behavior of $\hat{\eta}$ is consistent with all three models: bedforms were larger, on average, during the second than the first deployment, larger bedforms occurred during periods of low wave energy (May 12–15, June 17–21, June 29–July 3), and bedforms were minimal during periods of highest wave energy (May 9, May 15–17, June 21, June 28). Although our method of estimating \hat{k}_B is most subject to error when wave orbital velocities are high, negligible $\hat{\eta}$ were estimated for these conditions, consistent with the empirical formulae and observations of flat bed in the sonar images. In both the Nielsen and Styles and Glenn models ripple height depends on wave period (through ψ), which produces more variable predictions of ripple height than those of Wiberg and Harris. The Nielsen equations predict much larger bedform heights than the other two models under

conditions classified as suborbital. During the first week of the second deployment the range of $\hat{\eta}$ is closer to that predicted by Nielsen; however, during this period the data overpredict u_{*c} and z_{0a} for many bursts (Figure 6), suggesting that the \hat{k}_B estimates from this period may also be high. In general, the magnitudes of bedforms inferred from the data are more consistent with the predictions of Wiberg and Harris and Styles and Glenn than of Nielsen. 85% of the $\hat{\eta}$'s are less than 1.6 cm, which is the maximum ripple height predicted by the Wiberg and Harris equations.

4.4. Comparison with Sonar Images

The sonar images confirmed that the ripples present during the study were small in scale and that the types of bedforms present evolved over time (Figure 11). From the sonar images we assigned one of the four bedform categories to each time interval, and thus to each computed $\hat{\eta}$. We then computed the average $\hat{\eta}$ for each category. Mean $\hat{\eta}$ decreased with ripple type, when ripple type is ordered by increasing wave energy (Figure 19), consistent with the relationship between $\hat{\eta}$ and d_o (Figure 16). The shorter gray error bars in Figure 19, which show the 95% confidence interval on the means, do not overlap, indicating that the mean $\hat{\eta}$'s are significantly different between ripple type. On average, our method for estimating $\hat{\eta}$ detects differences in bedform height corresponding to the shifts between bedform categories. The long black error bars, which extend one standard deviation above and below the means, overlap considerably, indicating that within each ripple type $\hat{\eta}$ varied a great deal. Although megaripples are the largest bedform type, average $\hat{\eta}$ was smaller for mega- than linear or irregular ripples, because our estimates of $\hat{\eta}$ (equation 6) are based on the influence of small-scale ripples on hydrodynamic roughness. While the large-scale bedforms are clearly a response to hydrodynamic forcing, the influ-

Figure 19

ence of the large bedforms on hydrodynamics is not well understood. The small mean $\hat{\eta}$ for megaripples indicates that the large bedforms did not produce significant hydrodynamic roughness.

The energetic waves and small grain size at the site produce small bedforms compared to those found at LEO-15 [Traykovski *et al.*, 1999; Styles and Glenn, 2002]. At LEO-15 orbital ripples with wavelengths up to 1 m and heights up to 15 cm were observed. Styles and Glenn showed that a wave-current boundary layer model could be used to estimate roughness and bedform height of these relatively large bedforms. The anorbital and suborbital ripples present in this study, with expected heights of 1–2 cm, produce less hydrodynamic roughness than larger ripples and present a different set of conditions for testing the inverse method of estimating hydrodynamic roughness and bedform height. The time series of estimated \hat{k}_B show the expected response to wave energy and the estimated $\hat{\eta}$'s compare favorably with empirical predictions of bedform height, indicating that this type of inverse method can also be used to estimate hydrodynamic roughness and bedform height in high-energy wave environments where bedforms are small.

5. Conclusions

Velocity profiles measured with a PCADP in the bottom boundary layer were used to estimate bottom roughness and bedform height. The study took place on the inner shelf off the coast of Southwest Washington, at a mean depth of 9 m, during the spring and summer of 2001. Wave heights during the experiment ranged from 0.5 to 2 m, and current speeds ranged from 0 to 40 cm/s. Comparison of velocities measured by the PCADP and an ADVF mounted on the same tripod showed that the PCADP accurately measured burst mean speeds up to 40 cm/s and bottom orbital velocities up to 100 cm/s.

Burst means of horizontal velocities from the two instruments were highly correlated, with $R^2 > 0.97$.

Friction velocity u_{*c} and apparent bottom roughness z_{0a} were determined by fitting a logarithmic curve to the burst mean velocity profiles, following the law of the wall. For 873 of the 1579 PCADP bursts, R^2 exceeded 0.96 and burst mean speed at 50 cm above the bed was greater than 5 cm/s. The u_{*c} and z_{0a} values calculated from the velocity profiles corresponded well to values predicted by the Grant-Madsen wave-current boundary layer model. u_{*c} responded as expected to tidal and strong wind-driven currents. The Wiberg model [Wiberg *et al.*, 1994] was used to gauge the importance of stratification on u_{*c} . During peaks of both burst mean speed and bottom orbital velocity, a reduction in u_{*c} of approximately 0.5 cm/s (20%) was predicted due to stratification caused by sediment resuspension, but most of the time the predicted influence of stratification was negligible.

Sonar images showed that ripples, when present, were small in magnitude. Bedforms observed in the sonar images were classified into four categories corresponding to increasing levels of wave energy, and these categories varied as expected with wave height. Bed elevation profiles from the profiling sonar showed that large bedforms ($\lambda \sim 1$ m) developed when significant wave height reached approximately 1.5 m. This scale of bedform is not predicted by empirical ripple models.

GM was used iteratively to determine the hydrodynamic roughness length scale \hat{k}_B , by requiring convergence of the predicted u_{*c} to the value derived from the log fit of the data for each profile. \hat{k}_B was greatest during periods of low u_b and smallest during periods of high u_b , which is the expected response when roughness is dominated by form drag over bedforms. The logarithmic relationship between \hat{k}_B and wave orbital diameter was

used to develop a predictive relationship for k_B . The resulting time-varying k_{Bpred} was used to calculate u_{*cw} with GM. The result differed significantly from u_{*cw} calculated using a constant k_B , showing the importance of taking wave-driven variations in bottom roughness into account in modeling resuspension and transport.

Bedform height $\hat{\eta}$ was estimated from \hat{k}_B by subtracting the estimated roughness due to saltating sediment \hat{k}_{ST} and applying the relation between ripple height, ripple steepness, and bedform roughness proposed by *Grant and Madsen* [1982]. Roughness due to bedforms \hat{k}_{BF} was much larger than \hat{k}_{ST} or grain roughness k_N , except at times of greatest wave energy. The estimated $\hat{\eta}$'s decreased with increasing orbital diameter and compared well to ripple heights predicted by empirical formulae both in range and in temporal behavior. The mean estimated $\hat{\eta}$ varied significantly by bedform category, as determined from the sonar images. These results indicate that the estimation of hydrodynamic roughness and bedform height by iterative solution of a wave-current boundary layer model can be successful in high-energy wave environments where bedforms are small.

Acknowledgments. Thanks to Laura Kerr Landerman, Keith Kurrus, and Kevin Redman for help with data collection, and to Pat Wiberg and Dan Hanes for thoughtful reviews of an earlier version of this manuscript. This study was part of the Southwest Washington Coastal Erosion Study, a joint project of the U.S. Geological Survey and the Washington Department of Ecology which is funded by the U.S. Geological Survey. Any use of trade, product, or firm names in this paper is for descriptive purposes only and does not imply endorsement by the U.S. Government.

References

- Cacchione, D. A., and D. E. Drake, Shelf sediment transport: an overview with applications to the northern California continental shelf, in *The Sea, Volume Nine*, edited by B. LeMehaute and D. Hanes, chap. 21, pp. 729–773, John Wiley & Sons, 1990.
- Clifton, H., Wave-formed sedimentary structures - a conceptual model, in *Beach and nearshore sedimentation*, edited by R. Davis and R. Ethington, 24, pp. 126–148, Society of Economic Paleontologists and Mineralogists, 1976.
- Clifton, H., and J. Dingler, Wave-formed structures and paleoenvironmental reconstruction, *Marine Geology*, 60, 165–198, 1984.
- Drake, D. E., D. A. Cacchione, and W. D. Grant, Shear stress and bed roughness for combined wave and current flows over a rippled bed, *Journal of Geophysical Research*, 97, 2319–2326, 1992.
- Grant, W. D., and O. S. Madsen, Combined wave and current interaction with a rough bottom, *Journal of Geophysical Research*, 84, 1797–1808, 1979.
- Grant, W. D., and O. S. Madsen, Movable bed roughness in unsteady oscillatory flow, *Journal of Geophysical Research*, 87, 469–481, 1982.
- Gross, T., and A. Nowell, Mean flow and turbulence scaling in a tidal boundary layer, *Continental Shelf Research*, 2, 109–126, 1983.
- Hay, A., and D. Wilson, Rotary side-scan images of near-shore bedform evolution during a storm, *Marine Geology*, 119, 57–65, 1994.
- Jonsson, I., Wave boundary layers and friction factors, in *Proceedings of the 10th International Conference on Coastal Engineering*, pp. 127–148, ASCE, 1966.

- Lhermite, R., and R. Serafin, Pulse-to-pulse coherent Doppler sonar signal processing techniques, *Journal of Oceanic and Atmospheric Technology*, 1, 293–308, 1984.
- Li, M., and C. Amos, Predicting ripple geometry and bed roughness under combined waves and currents in a continental shelf environment, *Continental Shelf Research*, 18, 941–970, 1998.
- Madsen, O. S., Spectral wave-current bottom boundary layer flows, in *Proceedings of the 24th International Conference on Coastal Engineering*, pp. 384–398, ASCE, 1994.
- Madsen, O. S., L. Wright, J. Boon, and T. Chisholm, Wind stress, bed roughness and sediment suspension on the inner shelf during an extreme storm event, *Continental Shelf Research*, 13, 1303–1324, 1993.
- Neter, J., W. Wasserman, and M. Kutner, *Applied Linear Statistical Models*, Richard D. Irwin, Inc., 1985.
- Nielsen, P., Dynamics and geometry of wave-generated ripples, *Journal of Geophysical Research*, 86, 6467–6472, 1981.
- Nielsen, P., *Coastal bottom boundary layers and sediment transport*, World Scientific Publishing Co., 1992.
- Smith, J. D., Modeling of sediment transport on continental shelves, in *The Sea, Volume 6*, edited by E. Goldberg and Others, pp. 539–577, John Wiley & Sons, 1977.
- Styles, R., and S. Glenn, Modeling stratified wave and current bottom boundary layers on the continental shelf, *Journal of Geophysical Research*, 105, 24,119–24,139, 2000.
- Styles, R., and S. Glenn, Modeling bottom roughness in the presence of wave-generated ripples, *Journal of Geophysical Research*, 107, 10,1029–10,1044, 2002.

- Traykovski, P., A. Hay, J. Irish, and J. Lynch, Geometry, migration, and evolution of wave orbital ripples at LEO-15, *Journal of Geophysical Research*, *104*, 1505–1524, 1999.
- Wiberg, P., and C. Harris, Ripple geometry in wave-dominated environments, *Journal of Geophysical Research*, *99*, 775–789, 1994.
- Wiberg, P., and D. Rubin, Bed roughness produced by saltating sediment, *Journal of Geophysical Research*, *94*, 5011–5016, 1989.
- Wiberg, P., D. Drake, and D. Cacchione, Sediment resuspension and bed armoring during high bottom stress events on the northern California inner continental shelf: measurements and predictions, *Continental Shelf Research*, *14*, 1191–1219, 1994.
- Wikramanayake, P., and O. Madsen, Calculation of movable bed friction factors, *Technical Progress Report DACW-39-88-K-0047*, U.S. Army Corps of Engineers, Vicksburg, MI, 1991.
- Xu, J., and L. Wright, Test of bed roughness modles using field data from the Middle Atlantic Bight, *Continental Shelf Research*, *15*, 1409–1434, 1995.
- Zedel, L., A. Hay, R. Cabrera, and A. Lohrmann, Performance of a single-beam pulse-to-pulse coherent Doppler profiler, *IEEE Journal of Oceanic Engineering*, *20*, 290–297, 1996.

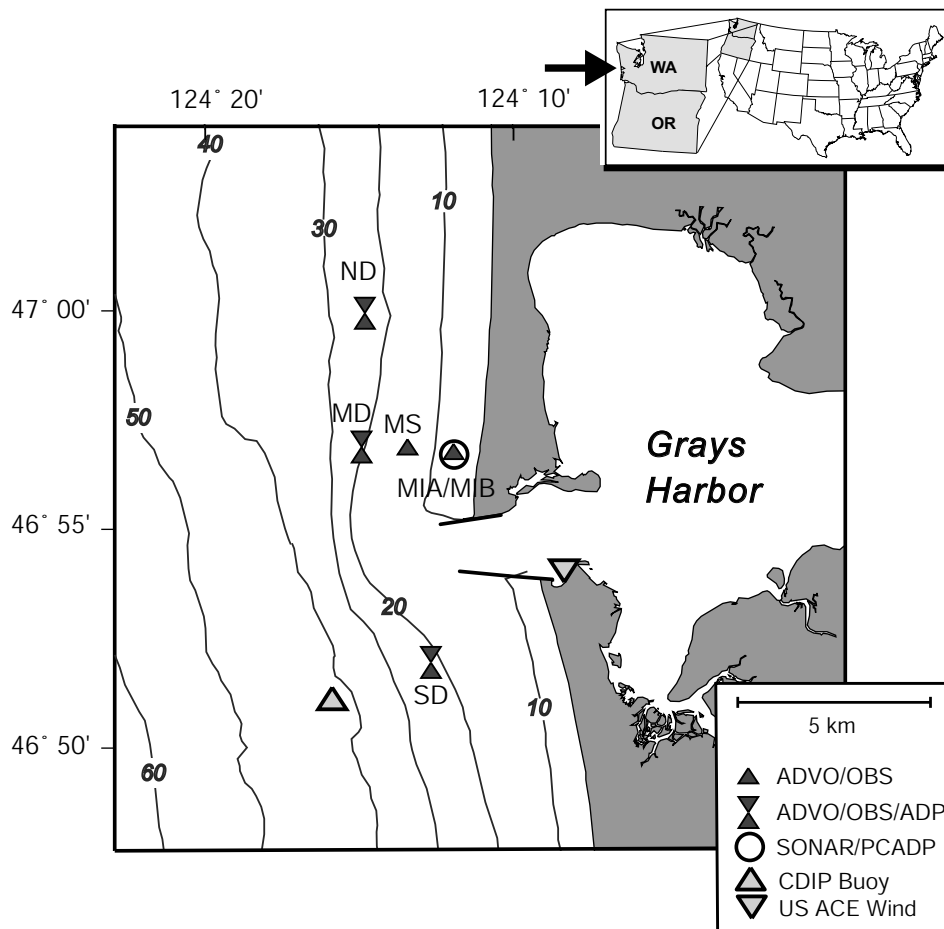


Figure 1. Chart of region offshore of Grays Harbor, WA. Contour interval 10 m. Data discussed in this paper were collected at sites MIA and MIB.

Parameter	Deployment 1	Deployment 2
No. cells	8	8
Cell size	10.8 cm	9.4 cm
Blanking distance	10 cm	10 cm
Profiling interval	1 s	1 s
Burst interval	3600 s	3600 s
Profiles per burst	1200	1200
Profiling lag	1.09 m	0.97 m
Resolution lag	0.49 m	0.49 m
Res. blanking distance	0.24 m	0.24 m
Max. hor. vel.	± 64 cm/s	± 72 cm/s
Max. hor. vel. w/ amb. res.	± 143 cm/s	± 143 cm/s
Pings per profile	9–10	13–15

Table 1. PCADP sampling parameters. Distances are vertical rather than along-beam.

Units are those used in PCADP commands. Number of significant figures is that provided in PCADP control file.

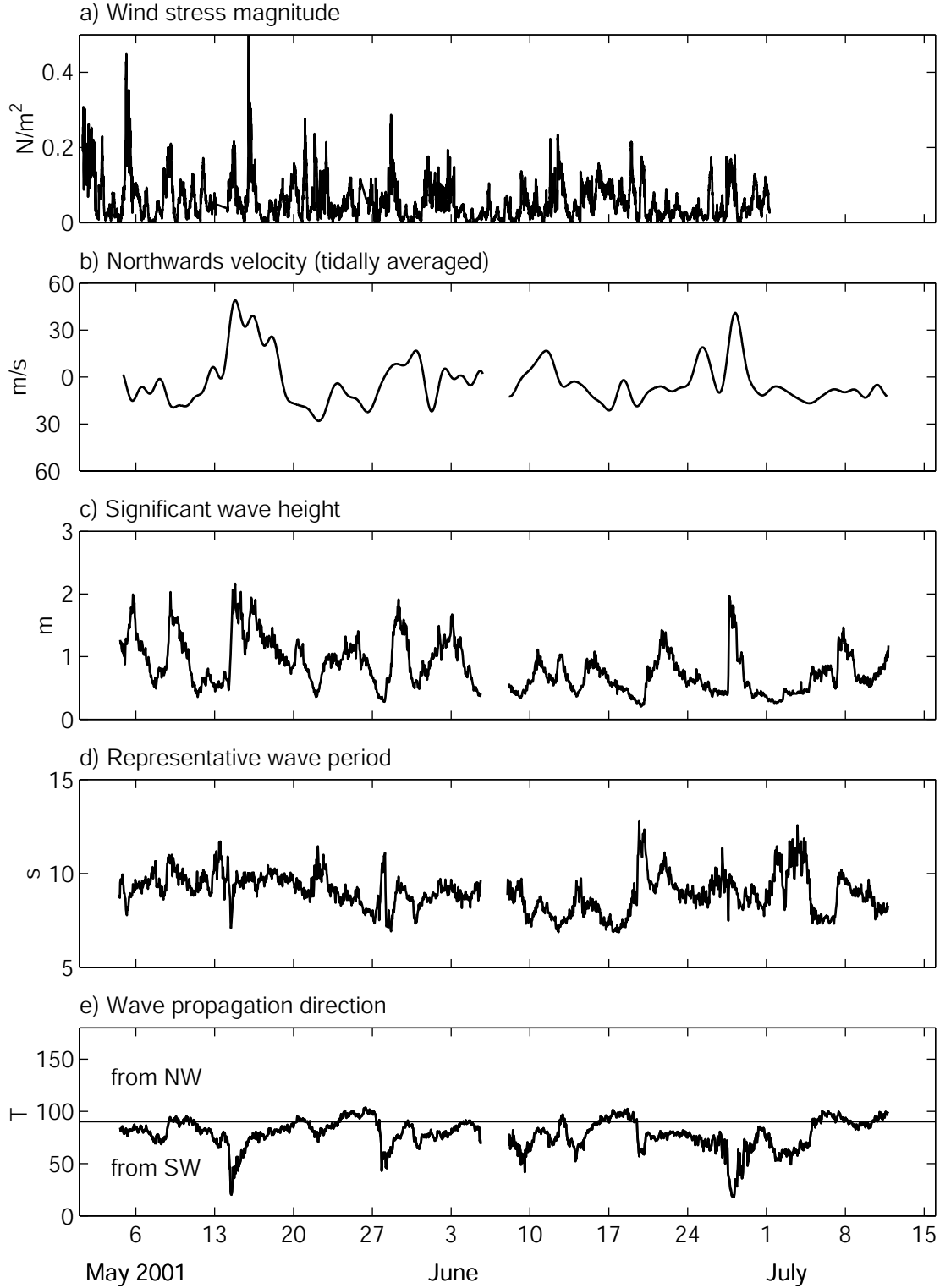


Figure 2. Conditions during the experiment: (a) Wind stress measured at Westport, WA. (b) Depth-averaged northwards velocity measured at Station MD (see Figure 1), low-pass filtered to remove tides. (c) Significant wave height, (d) representative wave period, and (e) wave direction at MIA.

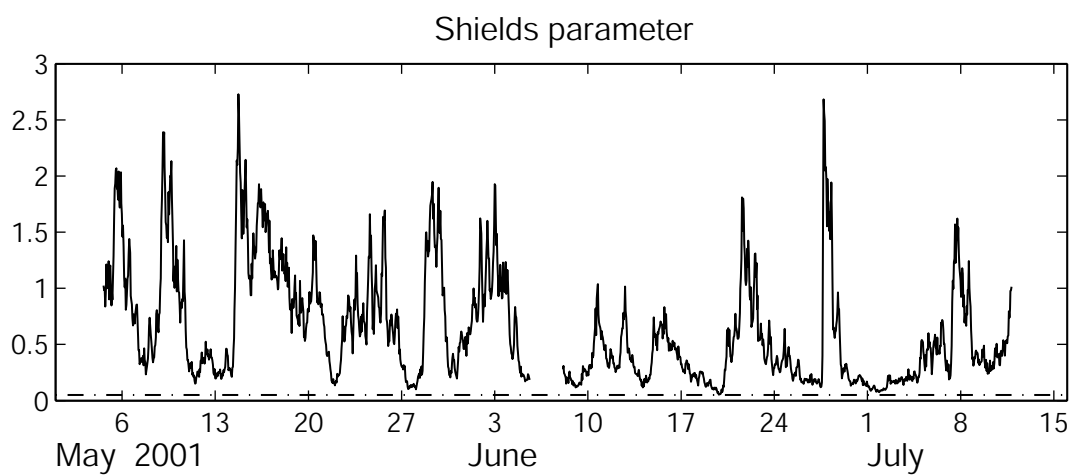


Figure 3. Shields parameter calculated from orbital diameter and Jonsson friction factor. Critical value for sediment resuspension shown by dash-dot line.

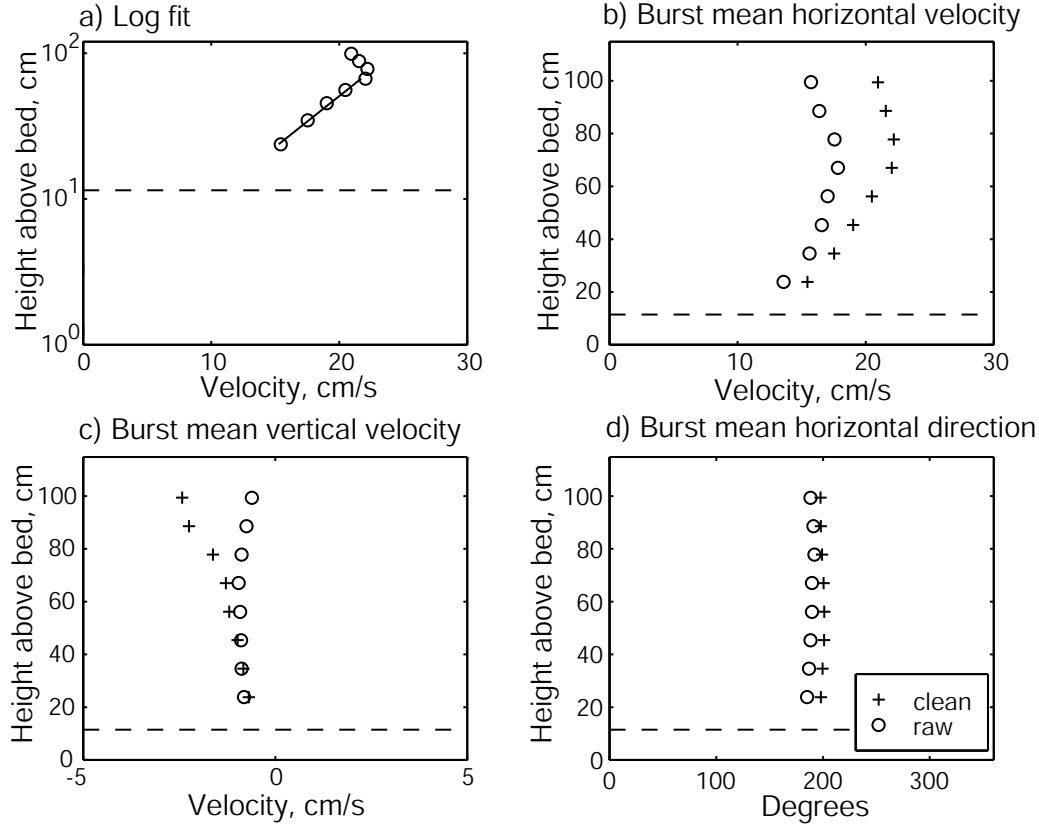


Figure 4. Example of burst mean profile measured by PCADP before and after ambiguity error correction: (a) Burst mean horizontal velocity vs. logarithm of height above bed, with logarithmic fit to bottom 5 bins. Profiles of (b) burst mean horizontal velocity; (c) burst mean vertical velocity; (d) current direction. Dashed line shows level below which reflection from the bottom is expected to interfere with velocity measurement.

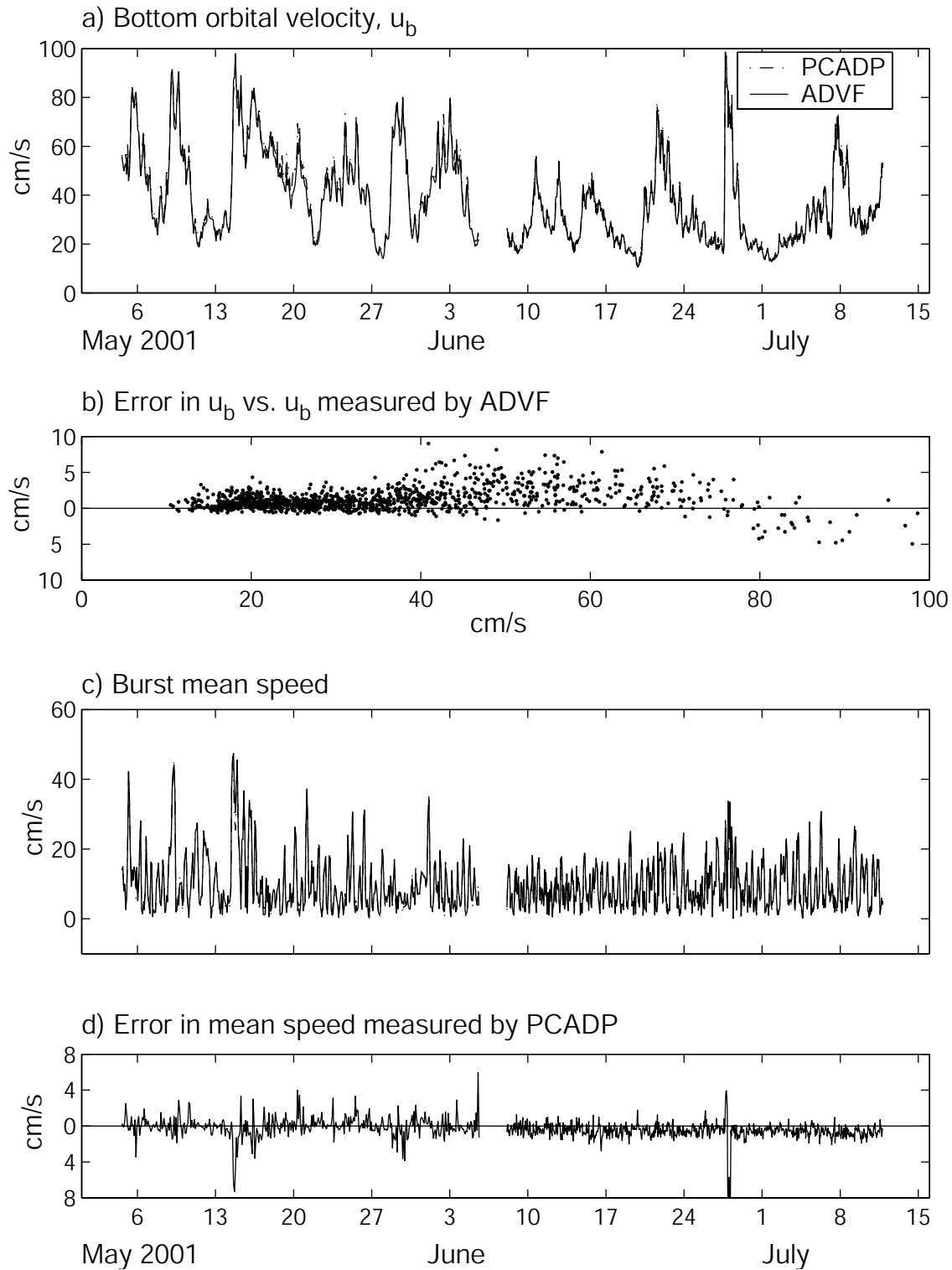


Figure 5. Time series of (a) bottom orbital velocity measured by the ADVF and PCADP cell 5; (b) relative error in bottom orbital velocity measured by the PCADP vs. bottom orbital velocity measured by the ADVF; (c) burst mean speed measured by the ADVF and PCADP cell 5; (d) relative error in burst mean speed measured by the

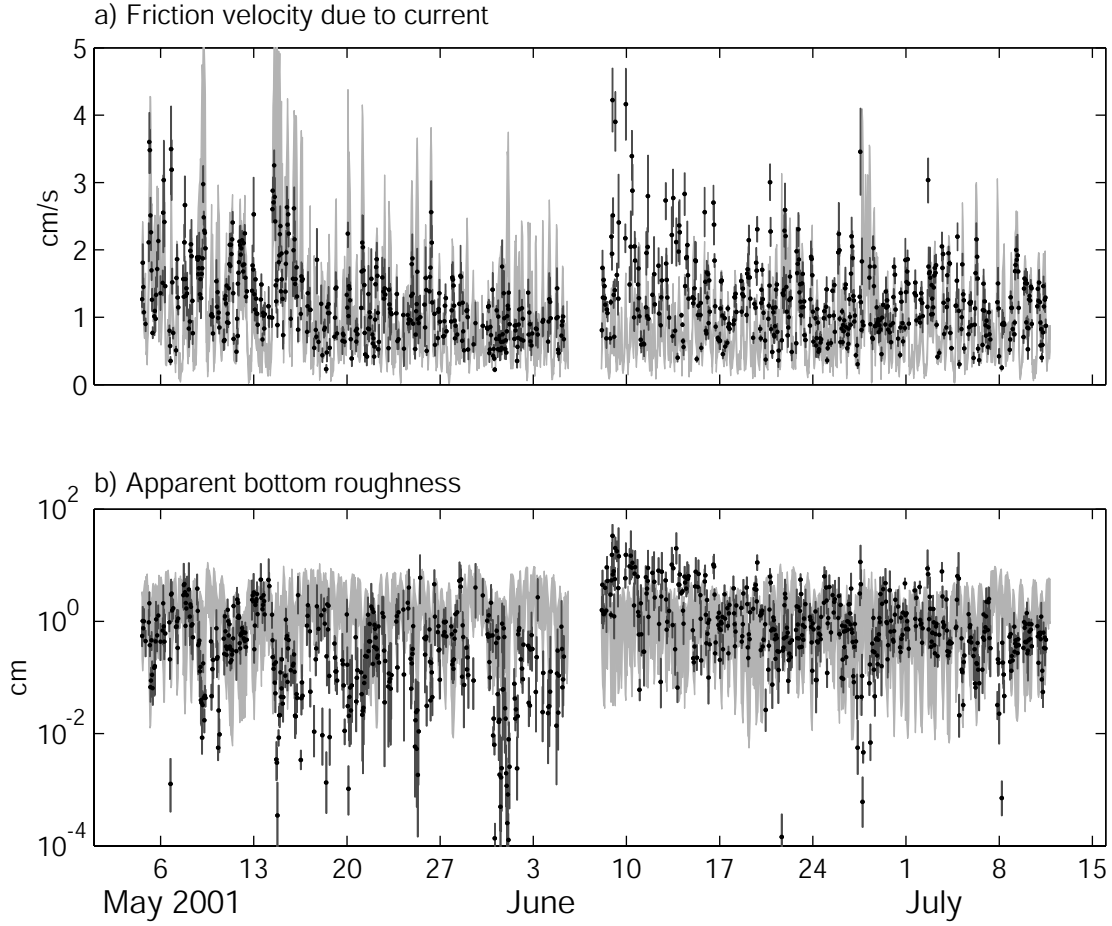


Figure 6. (a) Friction velocity due to current, and (b) apparent bottom roughness. Estimates from log fits of data are shown by black points, with dark grey error bars. Pale grey shaded region is bounded by Grant-Madsen model predictions with $k_B = 0.2$ mm and $k_B = 5$ cm.

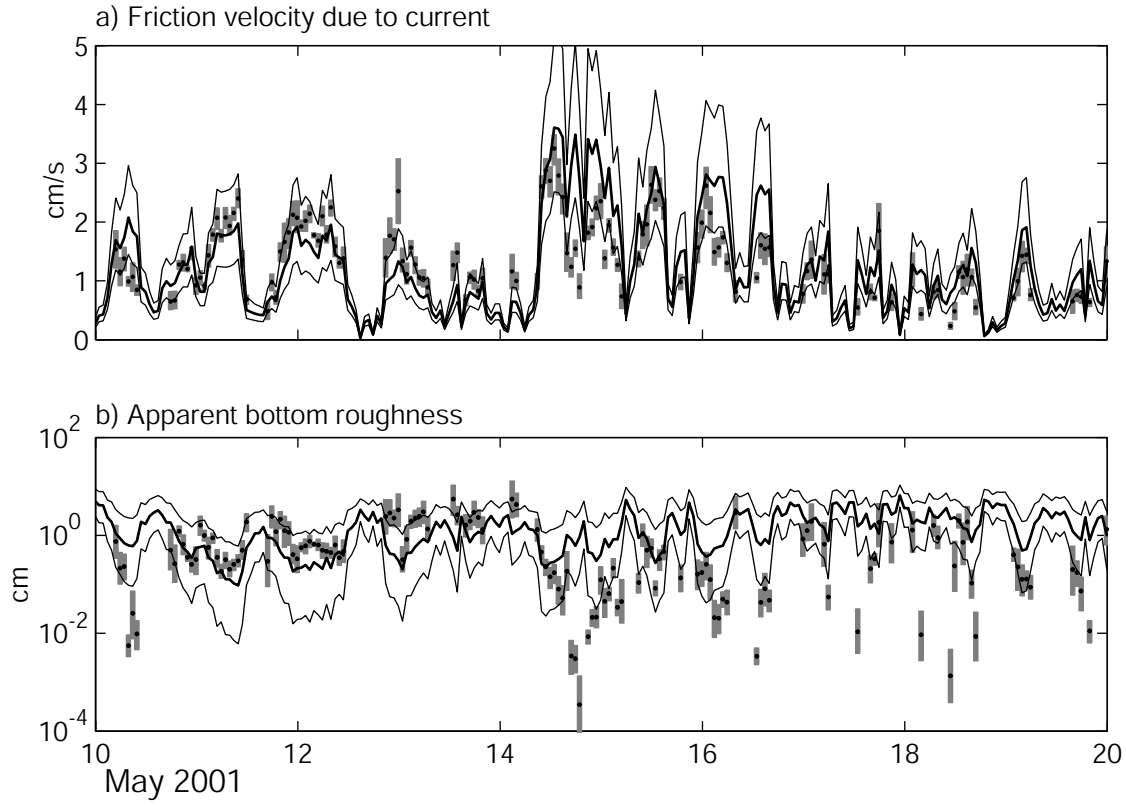


Figure 7. Detail of (a) u_{*c} and (b) apparent bottom roughness from log fits with 90% confidence limits for May 10–20. Thick line shows Grant-Madsen predictions with $k_B = 5$ mm, thin lines with $k_B = 0.2$ mm and $k_B = 5$ cm.

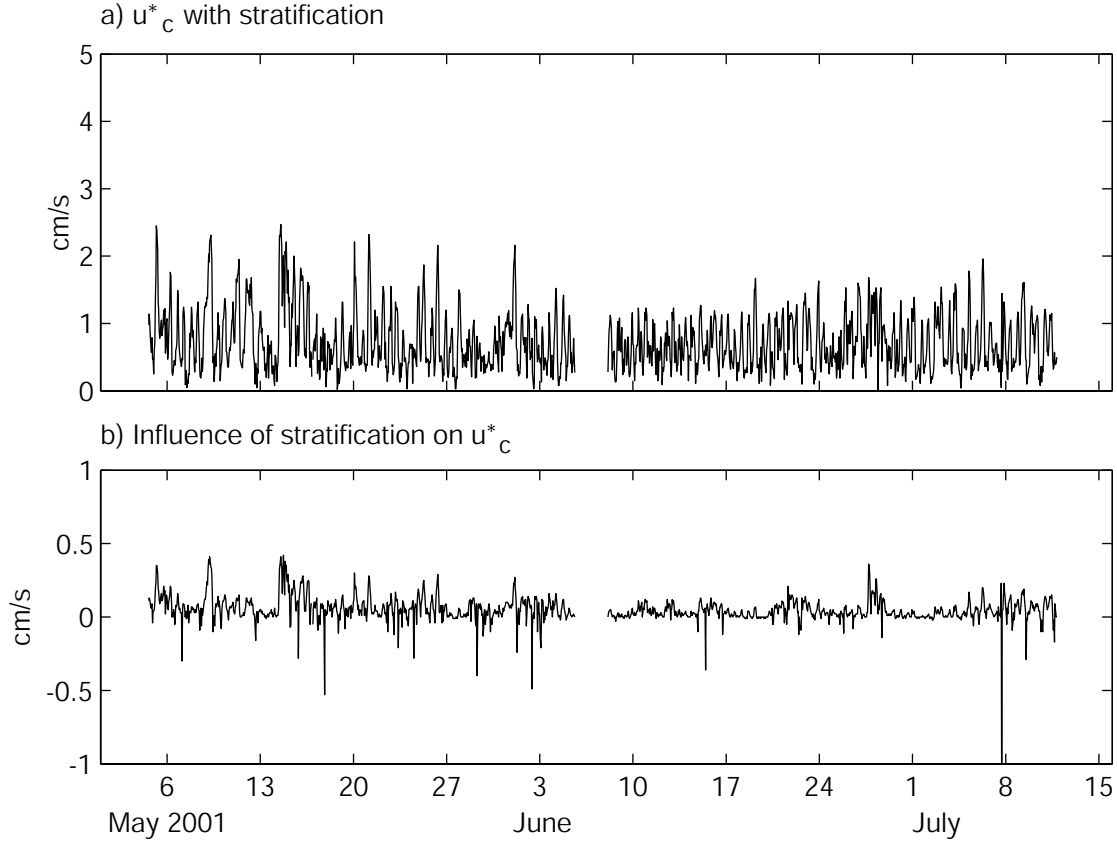


Figure 8. (a) Friction velocity due to currents u_{*c} , including the effect of stratification, predicted by the Wiberg model. (b) Difference between predicted u_{*c} without and with effect of stratification.

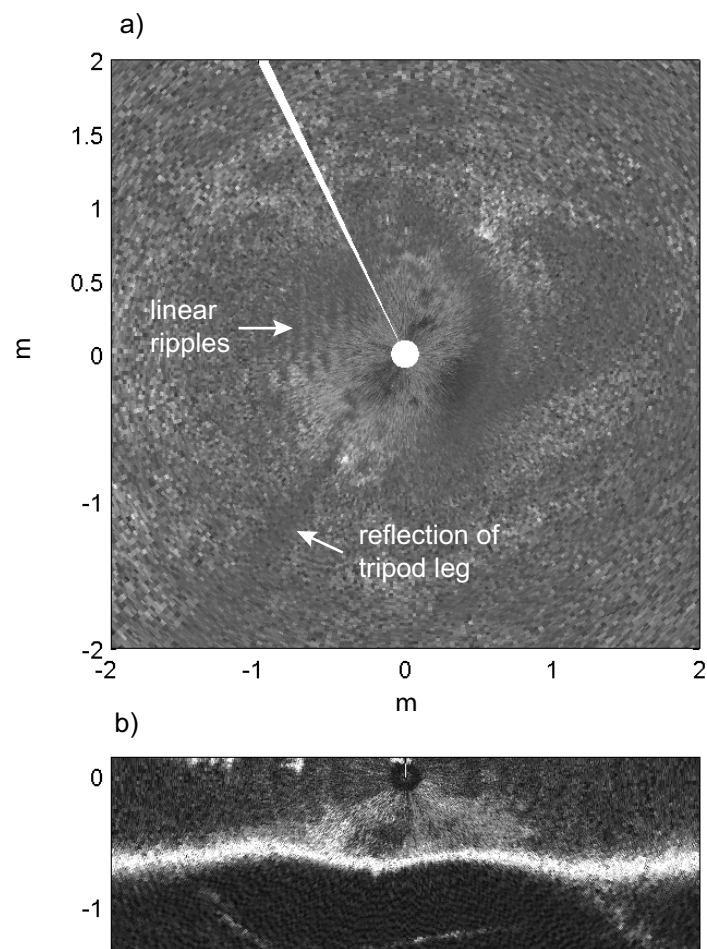


Figure 9. Sonar images from May 19 at 17:13: (a) Scanned, plan-view image; (b) profile image. Linear ripples can be seen in the left center of the plan-view image.

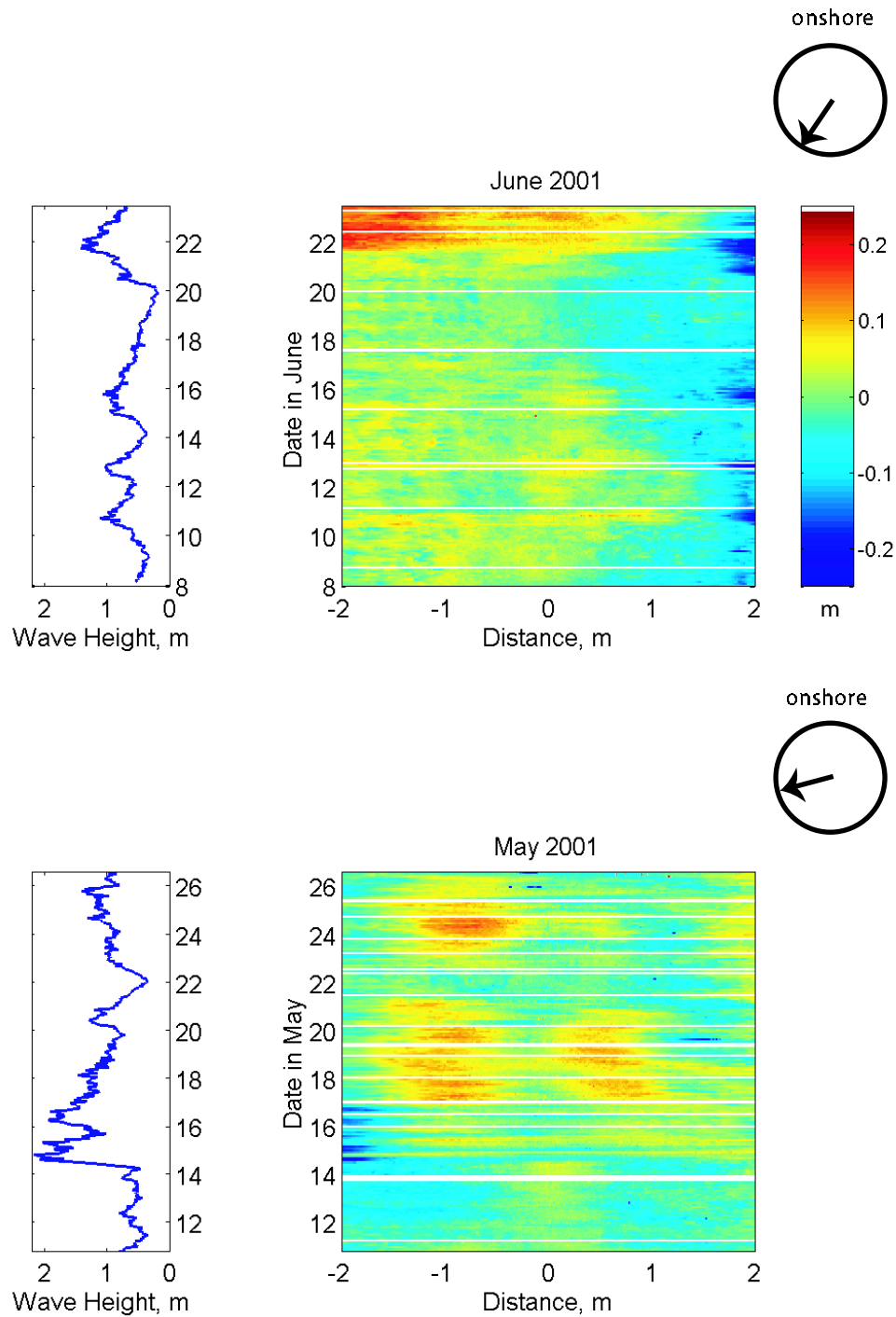


Figure 10. Time series of deviation of bed elevation from the mean, from profiling sonar images. Missing data indicated by white lines. 16 cm was added to profiles for June 8–10 to correct for settling. Arrows show onshore direction (270°) relative to horizontal in the bed elevation plots (i.e., May profiles are oriented 280° – 100° , June profiles are oriented

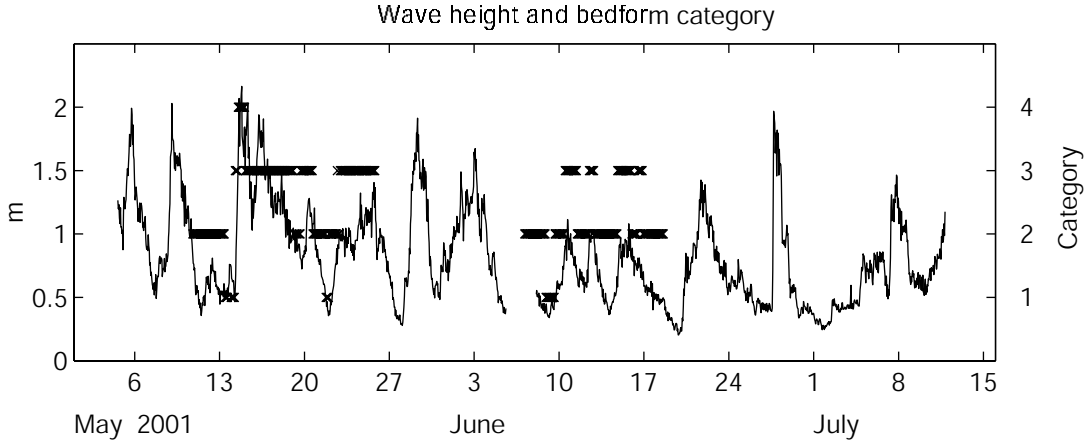


Figure 11. Bedform category from sonar images and significant wave height at MIA:

1 = linear ripples, 2 = irregular ripples, 3 = megaripples, 4 = flat bed.

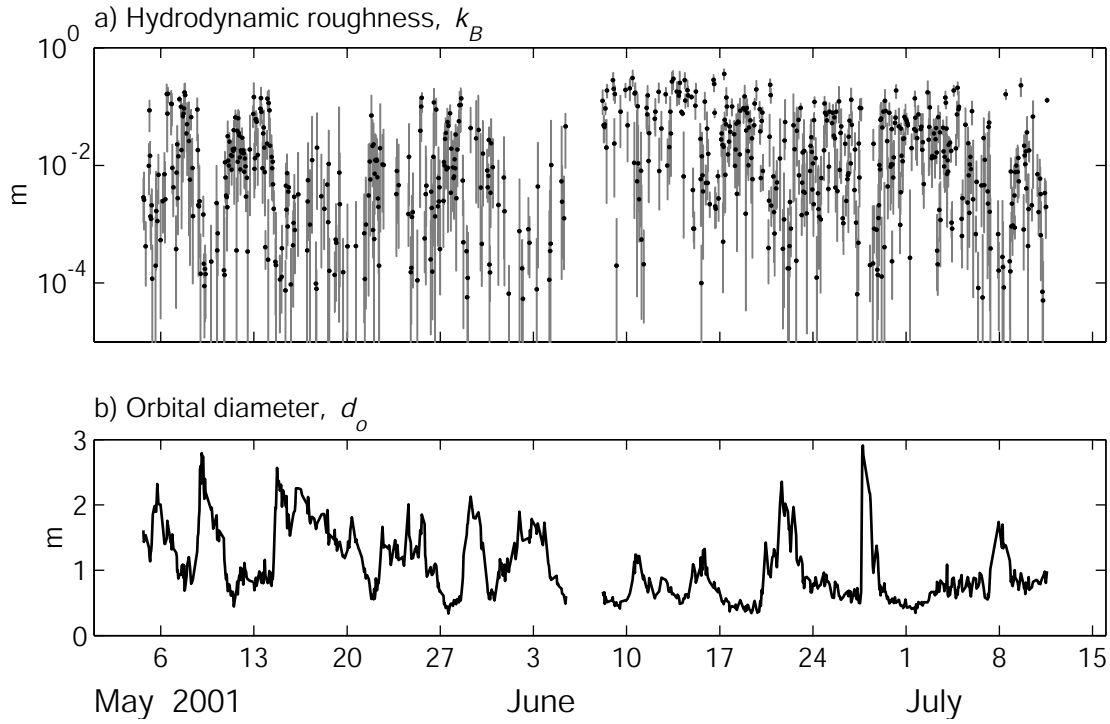


Figure 12. (a) Bottom roughness k_B and (b) wave orbital diameter. Limits on error bars for k_B calculated by using the upper and lower ends of the confidence interval on u_{*c} in the iterative solution of GM.

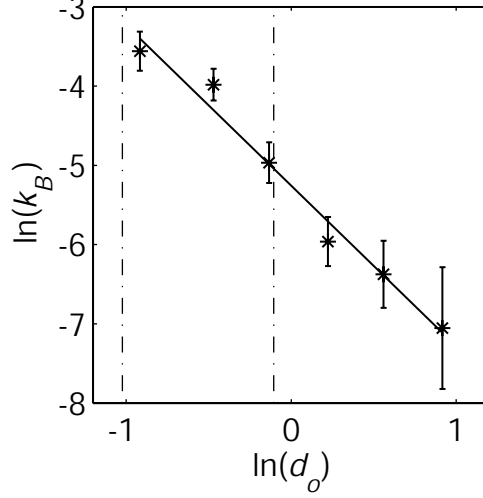


Figure 13. Logarithmic plot of geometric means (with 90% confidence intervals) of estimated roughness k_B vs. wave orbital diameter, and least-squares fit line. Dash-dot lines show predicted transitions from orbital to suborbital ripples (left) and from suborbital to anorbital ripples (right).

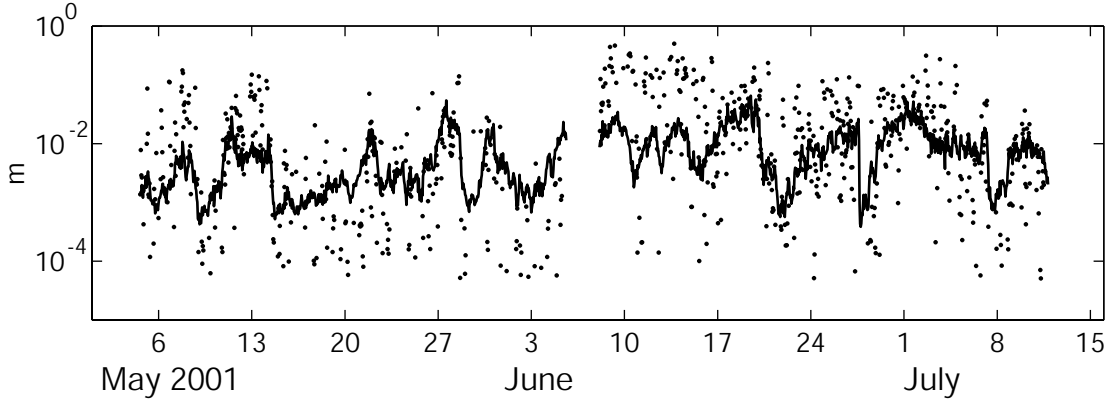


Figure 14. Bottom roughness \hat{k}_B estimated for individual bursts (dots) and time series of predicted $k_{B\text{pred}}$ calculated from log-linear relationship between wave orbital diameter and \hat{k}_B .

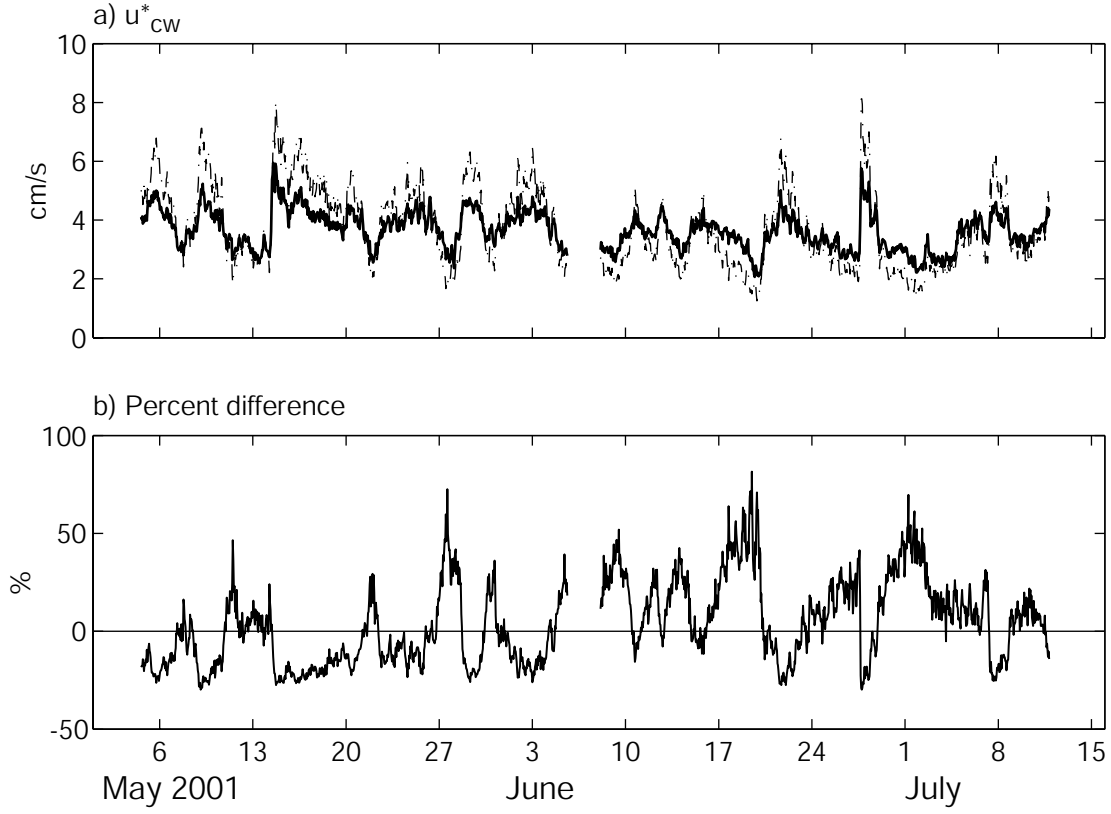


Figure 15. (a) Friction velocity due to waves and current calculated by GM with time-varying k_B (dark solid line) and with $k_B = 0.5$ cm (dash-dot line). (b) Percent difference between u_{*cw} calculated with time-varying and constant k_B .

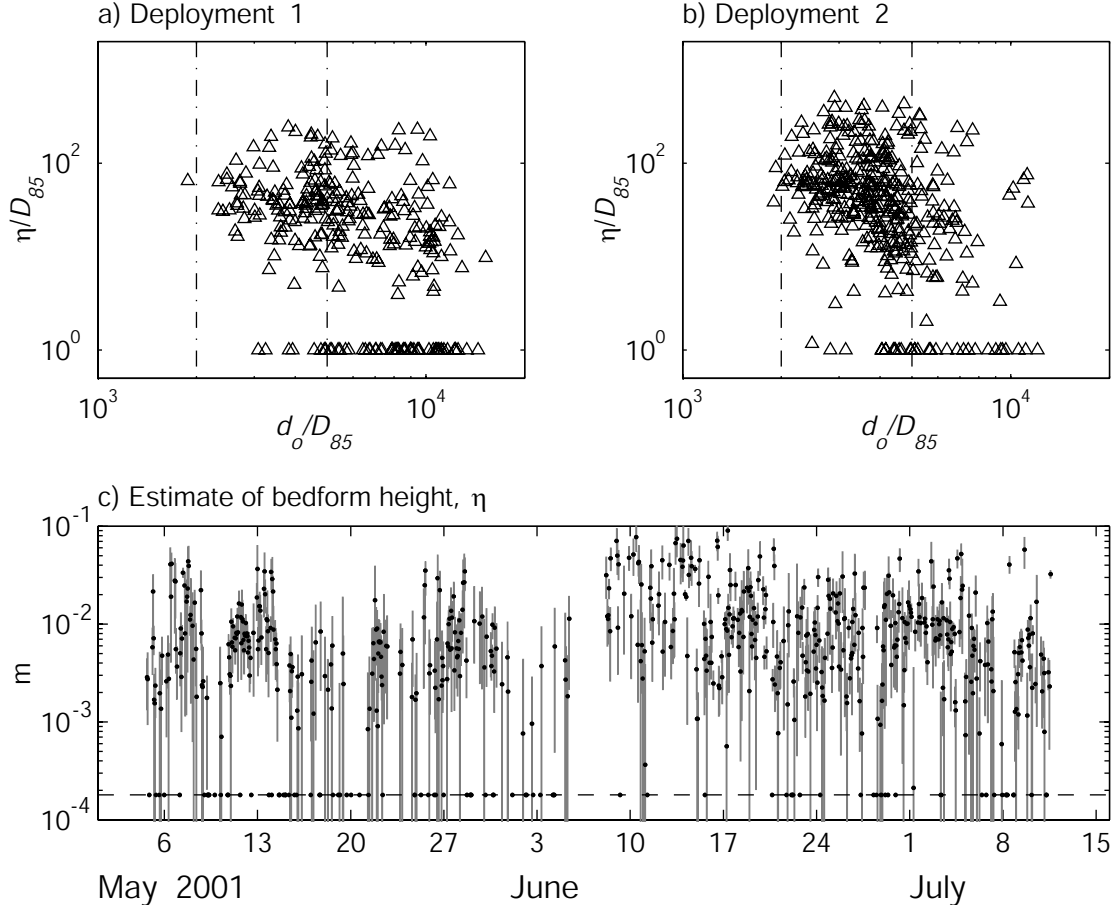


Figure 16. Estimated bedform height vs. orbital diameter, both scaled by grain size, for (a) deployment 1 and (b) deployment 2. Dash-dot lines show transition from orbital to suborbital (at $d_o/D = 2000$) and suborbital to anorbital (at $d_o/D = 5000$). (c) Bedform height estimated from equation 7. Dashed line is at D_{85} .

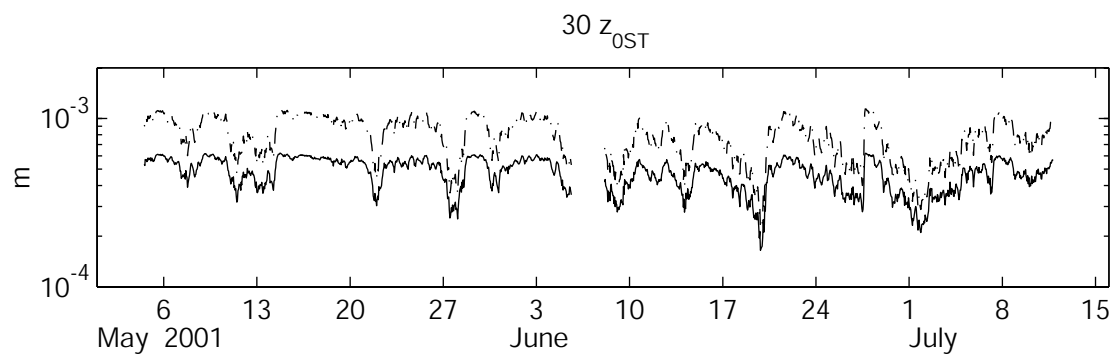


Figure 17. Roughness scale due to saltating sediment, based on Dietrich (dash-dot) and Wiberg and Smith (solid) formulations, multiplied by 30 for comparison with \hat{k}_B .

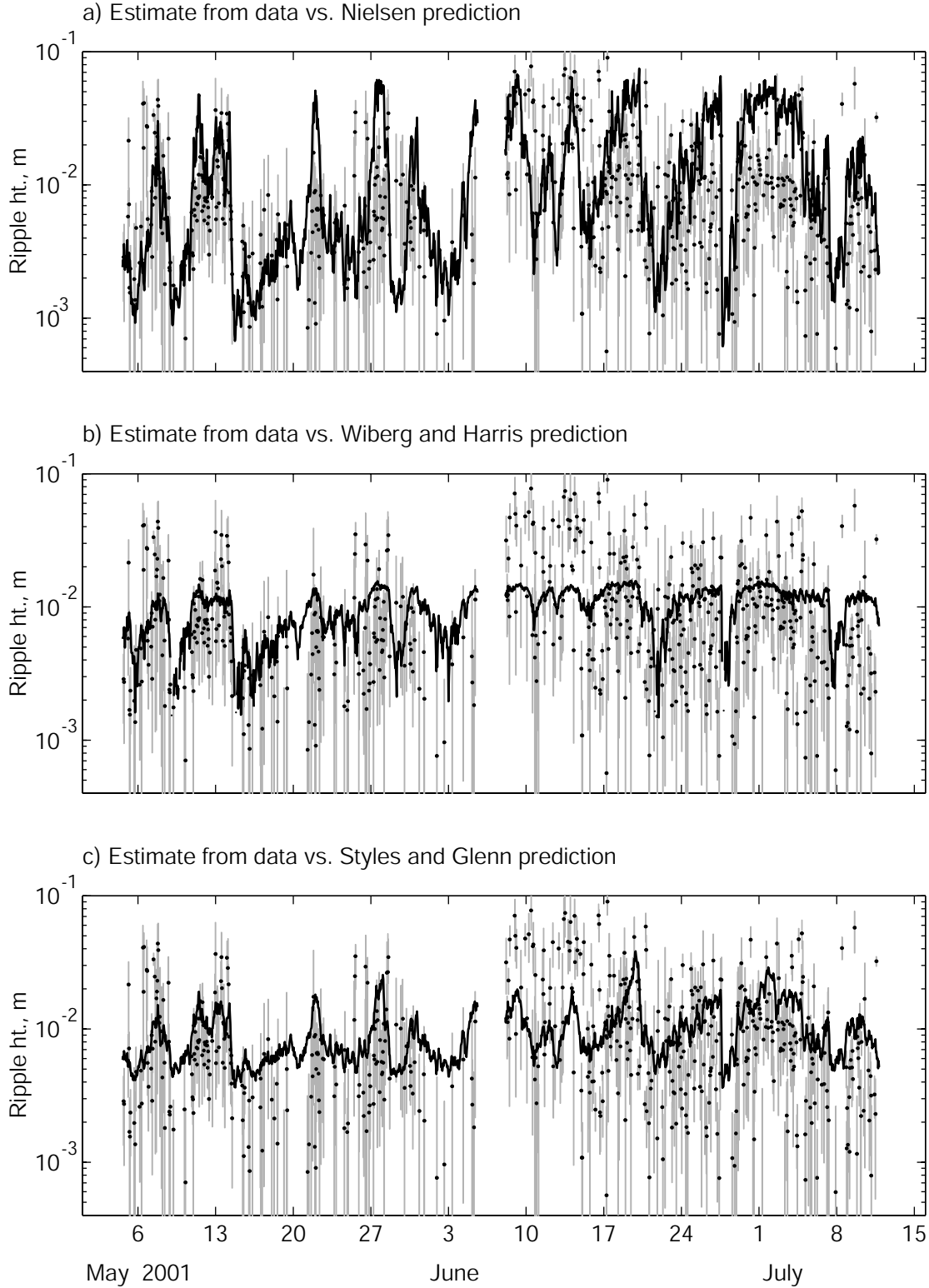


Figure 18. Ripple height estimated from data (dots) compared to predictions based on (a) *Nielsen* [1981], (b) *Wiberg and Harris* [1994], and (c) *Styles and Glenn* [2002].

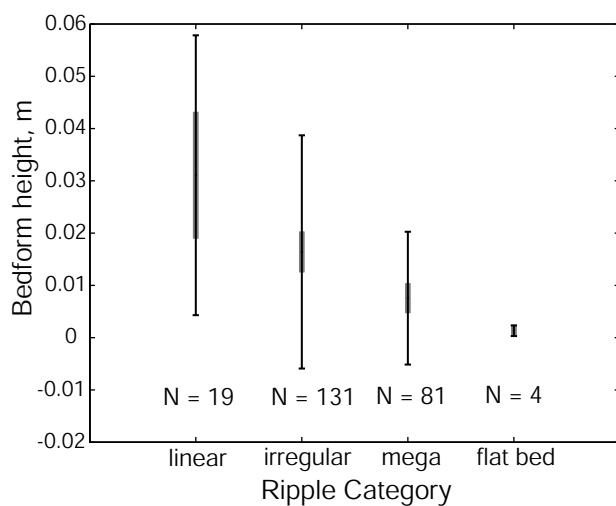


Figure 19. Bedform height estimated from \hat{k}_{BF} vs. ripple category. Long error bars are \pm one standard deviation, short error bars show the 95% confidence interval on the mean.